

# 3D Compressed Sensing for Highly Accelerated Hyperpolarized $^{13}\text{C}$ MRSI With In Vivo Applications to Transgenic Mouse Models of Cancer

Simon Hu,<sup>1,2</sup> Michael Lustig,<sup>3</sup> Asha Balakrishnan,<sup>4</sup> Peder E. Z. Larson,<sup>1</sup> Robert Bok,<sup>1</sup> John Kurhanewicz,<sup>1,2</sup> Sarah J. Nelson,<sup>1,2</sup> Andrei Goga,<sup>4</sup> John M. Pauly,<sup>3</sup> and Daniel B. Vigneron<sup>1,2\*</sup>

**High polarization of nuclear spins in liquid state through hyperpolarized technology utilizing dynamic nuclear polarization has enabled the direct monitoring of  $^{13}\text{C}$  metabolites in vivo at a high signal-to-noise ratio. Acquisition time limitations due to  $T_1$  decay of the hyperpolarized signal require accelerated imaging methods, such as compressed sensing, for optimal speed and spatial coverage. In this paper, the design and testing of a new echo-planar  $^{13}\text{C}$  three-dimensional magnetic resonance spectroscopic imaging (MRSI) compressed sensing sequence is presented. The sequence provides up to a factor of 7.53 in acceleration with minimal reconstruction artifacts. The key to the design is employing x and y gradient blips during a fly-back readout to pseudorandomly undersample  $k_x$ - $k_y$  space. The design was validated in simulations and phantom experiments where the limits of undersampling and the effects of noise on the compressed sensing nonlinear reconstruction were tested. Finally, this new pulse sequence was applied in vivo in preclinical studies involving transgenic prostate cancer and transgenic liver cancer murine models to obtain much higher spatial and temporal resolution than possible with conventional echo-planar spectroscopic imaging methods. *Magn Reson Med* 63:312–321, 2010. © 2009 Wiley-Liss, Inc.**

**Key words:** hyperpolarized  $^{13}\text{C}$ ; dynamic nuclear polarization; compressed sensing; magnetic resonance spectroscopic imaging; cancer

High polarization of nuclear spins in liquid state through hyperpolarized technology utilizing dynamic nuclear polarization has enabled the direct monitoring of  $^{13}\text{C}$  metabolites in vivo at a high signal-to-noise ratio (SNR) (1,2). Metabolic imaging studies thus far have focused on injecting hyperpolarized  $[1-^{13}\text{C}]$ pyruvate and observing its

uptake and conversion to  $[1-^{13}\text{C}]$ lactate,  $[1-^{13}\text{C}]$ alanine,  $^{13}\text{C}$ -bicarbonate, and  $^{13}\text{CO}_2$  (3–11). These studies have shown the potential of hyperpolarized technology for the metabolic imaging of cardiac disease (4,10,11) and cancer (5,7,8,12). The hyperpolarized cancer studies have demonstrated that in tumors the lactate dehydrogenase-catalyzed reaction involving pyruvate and lactate results in dramatically higher levels of hyperpolarized  $^{13}\text{C}$  lactate than in normal tissue (5,7,8,12). Mechanistically, lactate dehydrogenase catalyzes rapid exchange of the  $^{13}\text{C}$  label between pyruvate and lactate; thus, detected  $^{13}\text{C}$  lactate likely reflects the size of the preexisting endogenous lactate pool and lactate dehydrogenase expression (8).

Hyperpolarization of clinically relevant substrates other than  $[1-^{13}\text{C}]$ pyruvate is also an active area of research. Promising results have been reported for the hyperpolarization of  $[1-^{13}\text{C}]$ lactate (13),  $[5-^{13}\text{C}]$ glutamine (14), and  $^{13}\text{C}$  bicarbonate (15). Regardless of the specific in vivo application or substrate being hyperpolarized, the overriding limitation in dynamic nuclear polarization hyperpolarized spectroscopic imaging is the rapid decay of the hyperpolarized signal, which decreases exponentially with the spin-lattice  $T_1$  of the  $^{13}\text{C}$  nucleus (on the order of 30 to 70 sec for most substrates polarized). The hyperpolarized signal is also irretrievably lost due to saturation from radiofrequency excitation. These factors severely limit the number of phase encodes and thus the spatial resolution/coverage achievable, making accelerated imaging methods very important.

Our approach in this project was to apply compressed sensing, a recently developed technique based on random undersampling and a nonlinear reconstruction (16–19). Compressed sensing works well when underlying signals exhibit sparsity and have adequate SNR but may fail if those conditions are not met (20). The key design challenge in implementing compressed sensing for specific MRI applications is the development of pulse sequences and acquisition schemes that incorporate “incoherent” sampling, which is achieved by pseudorandom undersampling (20). In a prior study, an initial design incorporated pseudorandom undersampling in one spatial dimension into a spectroscopic imaging sequence to achieve 2-fold acceleration for 2-fold finer spatial resolution without increasing scan time (21). In this project, we advanced this compressed sensing methodology to two spatial dimensions and developed a 7.53-fold accelerated sequence for three-dimensional (3D) spectroscopic imaging, which was investigated through simulations, phantom testing, and in vivo

<sup>1</sup>Department of Radiology and Biomedical Imaging, University of California, San Francisco, San Francisco, California, USA.

<sup>2</sup>UCSF & UCB Joint Graduate Group in Bioengineering, University of California, San Francisco, San Francisco, California, USA.

<sup>3</sup>Department of Electrical Engineering, Stanford University, Stanford, California, USA.

<sup>4</sup>Department of Medicine, Division of Hematology/Oncology, University of California, San Francisco, San Francisco, California, USA.

Grant sponsor: National Institutes of Health; Grant number: R01 EB007588.

Grant sponsor: UC Discovery in conjunction with GE Healthcare; Grant number: ITL-BIO04-10148.

\*Correspondence to: Daniel B. Vigneron, PhD., Department of Radiology and Biomedical Imaging, Box 2512, University of California, San Francisco, 1700 4th St., QB3 Building, Suite 102, San Francisco, CA 94158-2512. E-mail: dan.vigneron@radiology.ucsf.edu

Received 12 June 2009; revised 17 August 2009; accepted 14 September 2009.

DOI 10.1002/mrm.22233

Published online 16 December 2009 in Wiley InterScience (www.interscience.wiley.com).

© 2009 Wiley-Liss, Inc.

experiments. In simulations, the limits of undersampling and the influence of noise on the compressed sensing nonlinear reconstruction were explored. We also applied this technique for hyperpolarized  $^{13}\text{C}$  imaging research in transgenic mice that express human oncogenes and develop liver cancer, a new animal model in which the higher spatial resolution is particularly beneficial.

## THEORY

### Compressed Sensing Literature

In essence, compressed sensing claims that signals that are sparse in some domain, not necessarily the time or frequency domains, can be recovered nearly perfectly even when sampled below the Nyquist rate. Candes et al. (16) and Candes and Romberg (18) gave the following illustrative example: a length  $N$  discrete signal consisting of  $M$  nonzero points can be recovered exactly from  $K$  pseudorandom Fourier measurements where

$$K \geq \text{Const} \cdot M \log N \quad [1]$$

and the solution is found by solving the convex minimization problem

$$\min \sum_n |g[n]| \quad \text{s.t.} \quad F_K \{g[n]\} = y \quad [2]$$

where  $F_K$  is the Fourier transform,  $g[n]$  is the proposed reconstruction of the length  $N$  discrete signal, and  $y$  are the  $K$  measured Fourier coefficients. The precise number of measurements needed (Eq. 1) depends strongly on the sparsity of the signal and weakly (logarithmic) on its size and generally (for most pseudorandom sampling patterns) falls well below the number of samples required by the Nyquist criterion. In practice, a reasonable way to determine the extent to which a signal can be undersampled is through simulation. Equation 2 states that the correct algorithm to reconstruct the undersampled signal consists of finding a solution  $g[n]$  with minimum  $\ell_1$ -norm in a sparse domain, with the constraint that it be consistent with the actual collected data (i.e., the Fourier coefficients of the reconstructed signal at positions where measurements occurred ( $F_K\{g[n]\}$ ) should match the actual measured coefficients  $y$ ). Real-world signals usually exhibit the most sparsity in some domain other than the object domain, e.g., the wavelet domain, in which case the  $\ell_1$ -norm of the wavelet transform of  $g[n]$  would be minimized (18–20). In addition, for real-world signals with noise, the data fidelity constraint is modified by allowing  $F_K\{g[n]\}$  to be within some noise standard deviations of  $y$ . Furthermore, as intuitively expected, reconstructions fail at very low SNR conditions where noise (in the sparse transform domain) dominates the signal (20). Again, the simulation approach was taken to evaluate the effects of noise. The last practical requirement, and the most important in terms of implementing compressed sensing for MRI, is that the undersampled measurements  $K$  be acquired in a pseudorandom pattern (20). This can be interpreted as requiring the aliasing from undersampling to spread out randomly and incoherently so that minimal interference with the underlying signal of interest occurs (20). In short, the practical

requirements for applying compressed sensing are (1) sparsity of the signal, (2) adequate SNR, and (3) random undersampling.

### Hyperpolarized Carbon-13 Signal

Hyperpolarized  $^{13}\text{C}$  MR spectroscopic imaging has several features that make it an excellent application for compressed sensing. First, hyperpolarized signals exhibit fundamental sparsity because typical spectra contain only a few peaks due to virtually no background interference from natural abundance carbon compounds (1,2). Second, with the >50,000-fold increase in signal due to hyperpolarization (1,2), spectra typically have high SNR. However, the rapid signal decay means data should be sampled quickly, i.e., in the limited time window during which SNR is high. Under conditions such as these, compressed sensing—a fast sampling strategy that works best for sparse and high SNR data—is very appropriate.

To verify that typical hyperpolarized spectra have sufficient sparsity for highly accelerated compressed sensing acquisitions, undersampling with various acceleration factors was simulated (in the absence of noise for the first simulation), and errors for the reconstructions were recorded. The reconstruction methodology (also described in the “Materials and Methods” section) was adopted from Lustig et al. (20). Briefly, the reconstruction software (based on SparseMRI: <http://www.mrsrl.stanford.edu/~mlustig/software/>) implemented a nonlinear conjugate gradient algorithm for the solution of the following optimization problem:

$$\underset{m}{\operatorname{argmin}} \|F_u(m) - y\|_2 + \lambda \|\psi(m)\|_1 + \alpha \text{TV}(m) \quad [3]$$

Equation 3 formulates Eq. 2 in so-called Lagrangian form, with the first term representing the data fidelity constraint in Eq. 2, the second term representing the  $\ell_1$ -norm in Eq. 2, and the third term representing a total variation penalty ( $\ell_1$ -norm of spatial finite-differencing) used to enforce some edge-preserving smoothness in the final solution (20). The weights given to  $\ell_1$ -norm minimization and smoothness can be manipulated by adjusting  $\lambda$  and  $\alpha$ , respectively, which also implicitly weights data fidelity.

The simulated data set shown in Fig. 1a was created by thresholding the peaks from a  $^{13}\text{C}$  phantom 3D magnetic resonance spectroscopic imaging (MRSI) acquisition to remove the noise and then giving the peaks line widths similar to those observed in phantom and animal experiments. The data dimensions for the simulated data set were  $64 \times 16 \times 16 \times 16$  in f/x/y/z, with three of the z slices containing spectra (Fig. 1a shows just one slice). The  $^{13}\text{C}$  simulations/phantom contained pyruvate, pyruvate-hydrate, alanine, and lactate—the metabolites observed in actual in vivo hyperpolarized spectra with  $[1-^{13}\text{C}]\text{pyruvate}$  as the injected substrate. This method for creating a simulated data set facilitated the replication of conditions from phantom experiments, including spatial resolution for testing of reconstruction of high spatial frequency components, making it straightforward to show that simulations matched experimental acquisitions with real MR hardware and pulse sequences. For these simulations,  $k_f\text{-}k_x\text{-}k_y$  ( $64 \times 16 \times 16$ ) were

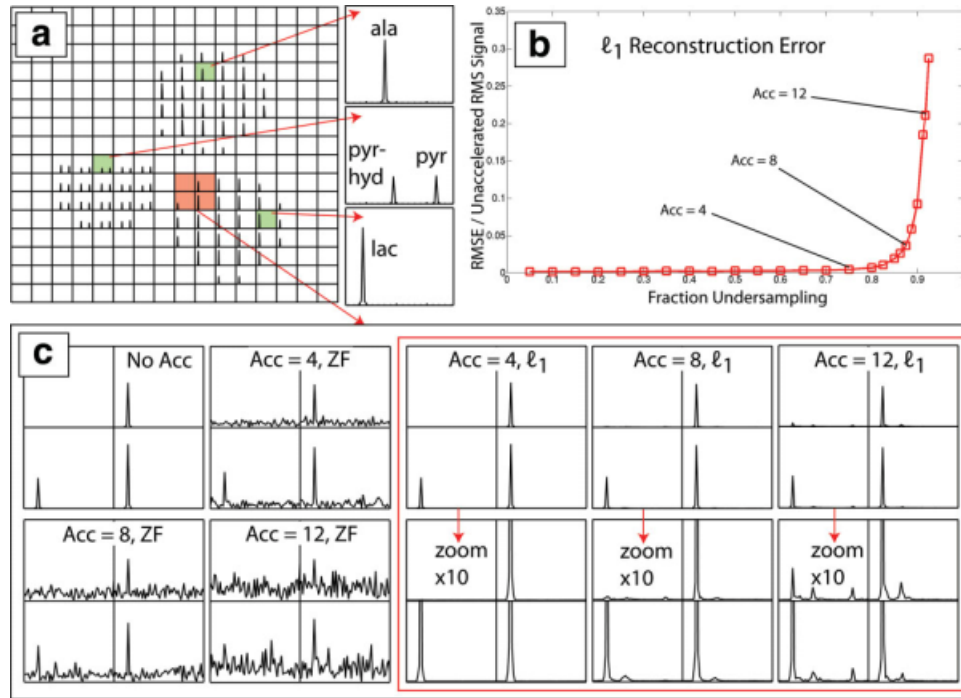


FIG. 1. **a**: Simulated data set created by thresholding the peaks from a  $^{13}\text{C}$  phantom 3D-MRSI acquisition to remove the noise and then giving the peaks a realistic line width. The data set contained three regions, each with different chemical species. **b**: The simulated data set was randomly undersampled with different undersampling factors, and  $\ell_1$  reconstructions were computed. The RMS errors between  $\ell_1$  reconstructed data and unaccelerated data were very low for a wide range of accelerations. **c**: Comparison of peaks from selected voxels. Zero-fill (linear) reconstructions exhibited incoherent aliasing that had a noiselike appearance and increased with higher undersampling.  $\ell_1$  nonlinear reconstructions with accelerations as high as 8 were nearly perfect. [Color figure can be viewed in the online issue, which is available at [www.interscience.wiley.com](http://www.interscience.wiley.com).]

undersampled in a pseudorandom fashion, except for the center  $64 \times 4 \times 4$  of  $k_x$ - $k_y$ , which were fully acquired. Fully sampling the high-energy/SNR center of  $k$ -space, i.e., variable density sampling, has been empirically determined to enhance compressed sensing reconstructions (20). The readout dimension,  $k_z$ , was fully sampled without lengthening scan time using an echo-planar fly-back scheme (described in the following sections). Figure 1b shows RMS errors between undersampled data sets and the original, with normalization by the root mean square (RMS) value for the original

$\left( \sqrt{\frac{1}{n} \sum_{i=1}^n (x_{\text{recon},i} - x_{\text{original},i})^2} / \sqrt{\frac{1}{n} \sum_{i=1}^n x_{\text{original},i}^2} \right)$ . As shown in Fig. 1b, increasing the undersampling increased the reconstruction error in the  $\ell_1$  compressed sensing reconstruction. The root mean square error (RMSE) for the  $\ell_1$  reconstruction rose rapidly, starting at approximately 85% undersampling, indicating that the reconstruction started to break down due to an insufficient number of  $k$ -space samples. Figure 1c shows a comparison of spectra from unaccelerated, zero-fill  $\times 4$  accelerated, zero-fill  $\times 8$  accelerated, zero-fill  $\times 12$  accelerated,  $\ell_1 \times 4$  accelerated,  $\ell_1 \times 8$  accelerated, and  $\ell_1 \times 12$  accelerated data sets. (Note: for the zero-fill reconstructions, density compensation was applied to the  $k$ -space points from undersampled regions. This was not needed for the compressed sensing acquisitions because the  $\ell_1$  algorithm synthesized the missing  $k$ -space data.) As expected, the

zero-fill reconstructed spectra exhibited incoherent aliasing demonstrating a noiselike appearance. The  $\ell_1$  nonlinear reconstruction removed this incoherent aliasing, as shown on the right side of Fig. 1c. As shown in Fig. 1c, the  $\times 4$  accelerated  $\ell_1$  reconstruction was practically perfect, and the  $\times 8$  accelerated  $\ell_1$  reconstruction yielded almost imperceptible distortions. The  $\lambda$  and  $\alpha$  parameters in Eq. 3 were chosen empirically (0.0005 and 0.0001, respectively) and over a reasonably broad range did not have a significant effect on reconstruction accuracy (data not shown). Note: the  $\lambda$  and  $\alpha$  values are those used in the SparseMRI software package (20) (<http://www-mrsrl.stanford.edu/~mlustig/software/>); in other words, they are the  $\lambda$  and  $\alpha$  weights in Eq. 3 when the object domain signal ( $m$ ) is normalized to have unity magnitude. The practical limitations of compressed sensing have been documented (18–20), but these application-specific simulations with realistic data and concrete matrix sizes are important to provide a sense of the range of feasible accelerations.

The second set of simulations dealt with noise. The top left corner of Fig. 2a shows the noiseless slice data from Fig. 1a. The three rows show the alanine, pyruvate/pyruvate-hydrate, and lactate regions, respectively. The first column of Fig. 2a gives an example of magnitude spectra before undersampling, with additive white gaussian noise added such that the maximum signal voxel had an SNR of 50 (SNR defined as the magnitude peak height divided by the SD in the magnitude noise signal). The second column shows magnitude spectra after factor

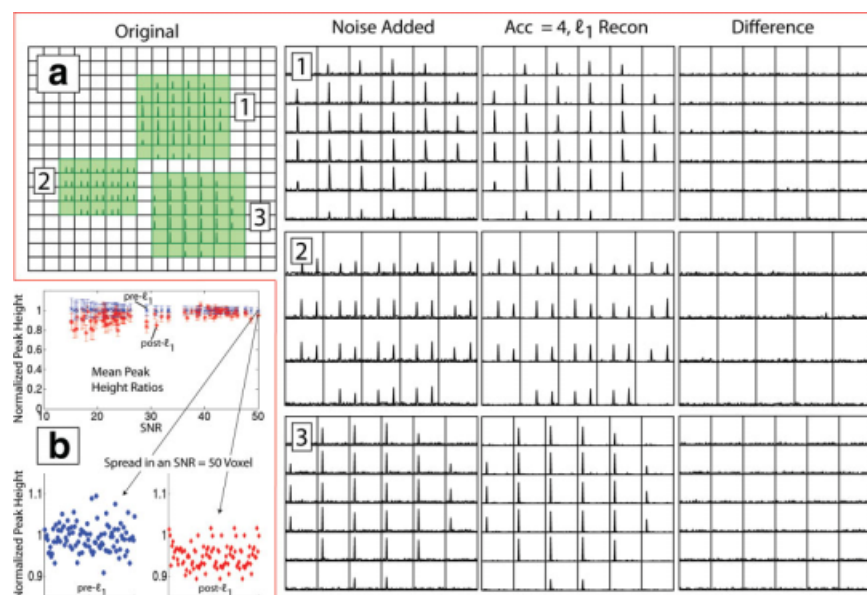


FIG. 2. **a:** Reproduction of the noiseless data set from Fig. 1a. The three regions containing (1) alanine, (2) pyruvate/pyruvate-hydrate, and (3) lactate, respectively, are highlighted. On the right side, in the first column, those three sets are shown again but with additive white gaussian noise added. In the second column, an  $\ell_1$  reconstruction with factor of 4 undersampling of the noisy data is shown. The third column shows the magnitude difference. **b:** The noise simulation in part (a) was run 100 times, with distinct noise patterns each time. For each of the peaks across the many voxels, and for both the noise added (pre- $\ell_1$ ) and noise added with factor of 4 undersampling with  $\ell_1$  reconstruction (post- $\ell_1$ ) data sets, the mean/SD of the ratio of peak height to true noiseless peak height was plotted. All pre- $\ell_1$  ratios were centered on unity regardless of signal strength, but the post- $\ell_1$  ratios were slightly skewed downward for peaks that had low starting SNR. The bottom part shows a scatterplot of pre- $\ell_1$  and post- $\ell_1$  peak height to true noiseless peak height ratios for a selected peak over the 100 runs. [Color figure can be viewed in the online issue, which is available at [www.interscience.wiley.com](http://www.interscience.wiley.com).]

of 4 random undersampling and an  $\ell_1$  reconstruction using the same parameters as in the first set of simulations. The last column gives the magnitude difference between the first two columns. The noisy data and the  $\ell_1$  reconstructed data agreed very well, with most peaks in the undersampled data set reproduced accurately. For each peak in each voxel, the ratios for noise-added peak height over noiseless true peak height (pre- $\ell_1$ ) and  $\ell_1$ -reconstructed peak height over noiseless true peak height (post- $\ell_1$ ) were computed, and the noise simulation was run 100 times, with distinct random noise patterns each time. The means/standard deviations for the pre- $\ell_1$  and post- $\ell_1$  ratios for every peak were then computed and plotted (top of Fig. 2b). A mean close to unity signifies agreement on average with true peak height, which, as shown by the blue x marks in the top of Fig. 2b, was the case for all noisy peaks regardless of SNR before the  $\ell_1$  reconstruction. The red stars in the top of Fig. 2b show the post- $\ell_1$  mean ratios for all peaks in the data, with values for high SNR peaks (SNR >25 after adding additive white gaussian noise and before undersampling) coming close to unity ( $0.96 \pm 0.04$ ) and those for lower SNR peaks (SNR <25) systematically reduced slightly ( $0.91 \pm 0.07$ ). (Note: in order to make the comparisons between unaccelerated and accelerated data sets equal in terms of SNR, the SNR for the  $\ell_1$  runs was scaled up to adjust for the SNR lost from undersampling.) The bottom of Fig. 2b illustrates reconstruction variability in peak ratios over 100 runs for a particular peak in a particular voxel, specifically the SNR 50 peak, whose peak height means are indicated in the top of Fig. 2b. The reduced peak ratios are most likely

due to a slight bias in the  $\ell_1$  reconstruction itself. Specifically, it was shown that  $\ell_1$ -norm minimization is equivalent to iterative soft thresholding, which has a bias toward shrinking detected components (22). One possible future way to reduce the bias could be to try newer compressed sensing reconstructions, such as an iteratively reweighted  $\ell_1$  method proposed by Candes et al. (23)

## MATERIALS AND METHODS

### Random Undersampling Pulse Sequence Design for $^{13}\text{C}$ Fly-Back 3D-MRSI

To implement compressed sensing for MRSI, the main design challenge was to incorporate random undersampling into a practical pulse sequence. The starting point was a double spin-echo  $^{13}\text{C}$  sequence (24) with phase encoding in x and y and a fly-back echo-planar spectroscopic imaging readout (25) in z and frequency. (In the fly-back readout, the time between fly-back lobes controlled spectral bandwidth, and the number of lobes in conjunction with spectral bandwidth determined the spectral resolution possible.) To take advantage of the sparsity in hyperpolarized data, as was done in the simulations, a way was needed to undersample three  $k$ -space dimensions, including the frequency dimension (containing sparse spectra) but excluding the fully sampled  $k_z$  echo-planar spectroscopic imaging readout dimension. To accomplish this, we employed the design trick of placing gradient blips during the rewind portions of the fly-back readout to randomly hop around in  $k$ -space (21). Figure 3a shows the complete pulse sequence



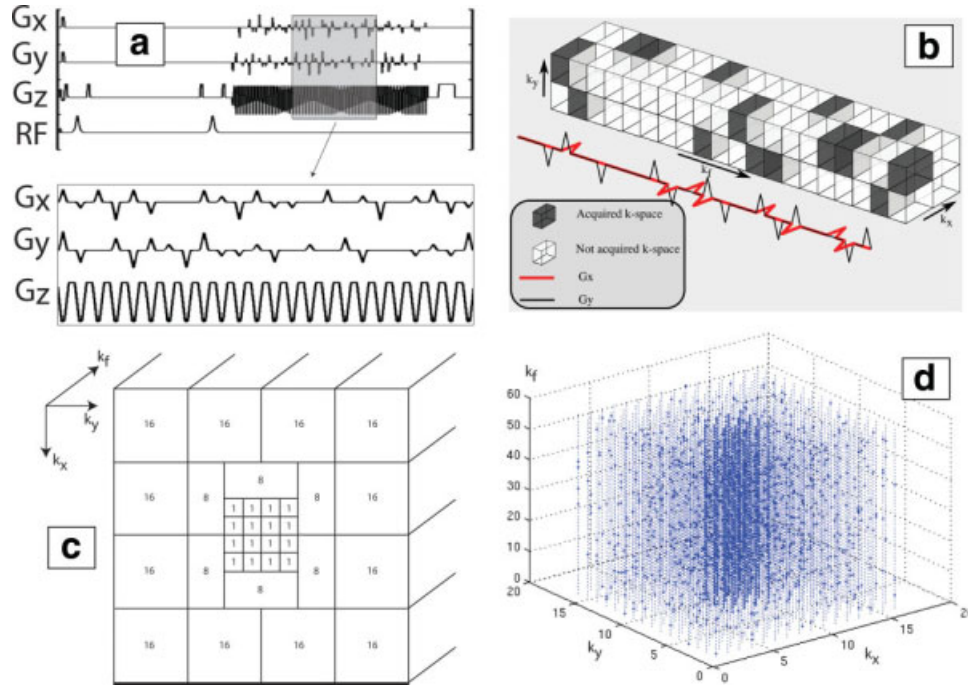


FIG. 3. **a:** Compressed sensing 3D-MRSI pulse sequence. Phase encode localization occurred in x/y with fly-back readout in z/f. Full echo data were collected by using twin adiabatic refocusing pulses. The key design trick was placing x/y gradient blips during the rewind portions of the fly-back readout. The blip areas were integer multiples of phase-encode steps, allowing for hopping around and random undersampling of  $k_f$ - $k_x$ - $k_y$  space. **b:** Illustration of random undersampling of a swath of  $k_f$ - $k_x$ - $k_y$  space using blips. The blips portioned out the acquisition over several lines in  $k$ -space during one pulse repetition time. **c:** Depiction of variable density sampling resulting in a  $\times 7.53$  accelerated sequence. Central regions of  $k$ -space were fully sampled, middle regions undersampled by a factor of 8, and outer edges undersampled by a factor of 16. **d:** Resulting random undersampling pattern in  $k_f$ - $k_x$ - $k_y$ . [Color figure can be viewed in the online issue, which is available at [www.interscience.wiley.com](http://www.interscience.wiley.com).]

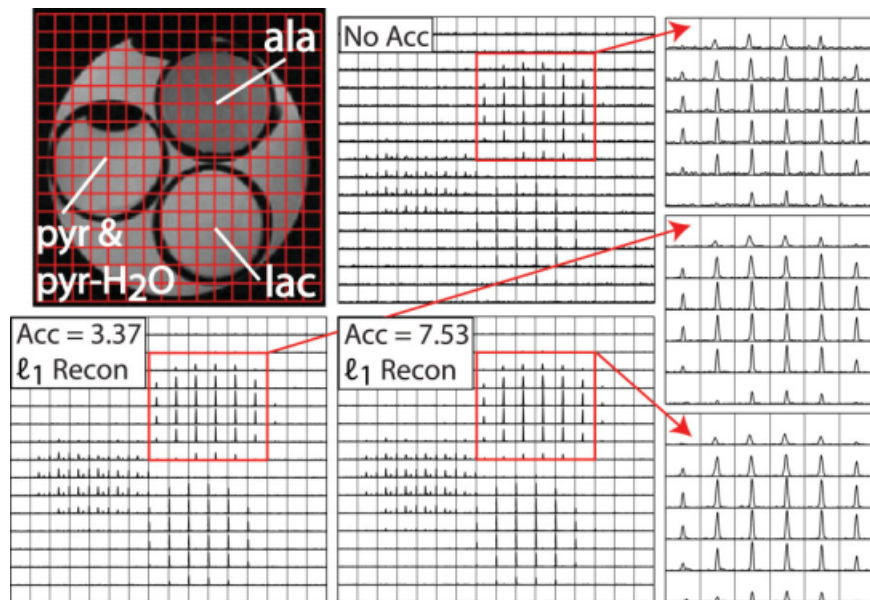
with double spin-echo adiabatic refocusing pulses, fly-back readout, and x and y gradient blips. (Note: the x and y gradient waveforms have been zoomed in vertically for viewing purposes.) Figure 3b illustrates how such a blipped scheme can provide random undersampling of  $k_f$ - $k_x$ - $k_y$  space. In Fig. 3b, the area of each x or y gradient blip equals the area in an x or y phase encode increment. In other words, Fig. 3b shows a  $\text{num\_lobes} \times 2 \times 2$  region of  $k_f$ - $k_x$ - $k_y$  space where  $k_f$  data are read as time progresses and each x or y gradient blip moves the reading of  $k_f$  data up or down one phase encode step in  $k_x$  and  $k_y$ , respectively. With the use of pseudorandomly placed up/down x and y gradient blips, a region of  $k_f$ - $k_x$ - $k_y$  space covering  $2 \times 2$  phase encodes can be randomly undersampled in the time of one pulse repetition time—a factor of 4 acceleration. For a  $16 \times 16$  phase encode matrix with a fully sampled  $4 \times 4$  central region, the total acceleration would be  $\frac{16 \times 16}{4 \times 4 + (16 \times 16 - 4 \times 4)/4} \approx 3.37$ , which is slightly less than 4. The use of the blipped design trick accomplished the counterintuitive goal of skipping around and undersampling in the time ( $k_f$ ) dimension itself. If blip areas were allowed to equal the area of two or more phase encode steps, then even larger  $k_x$ - $k_y$  blocks could be undersampled and acceleration increased. Thus, to undersample an  $m \times n$  block of  $k_x$ - $k_y$  space, the x and y gradient blips must go up to the areas of  $m - 1$  and  $n - 1$  phase encode increments, respectively. Figure 3a and c illustrates this idea by showing blips of three different amplitudes and  $2 \times 4$ ,  $4 \times 2$ , and  $4 \times 4$   $k_x$ - $k_y$  blocks. The

design in Fig. 3c produces the random undersampling pattern shown in Fig. 3d, which resulted in an acceleration factor of 7.53. The methodology presented here, with the addition of blips on multiple gradient axes and arbitrary blip areas, significantly advanced our initial design method in which acceleration was limited to a factor of 2. Experimental validation of these new designs is described in the following sections.

#### Hardware and Pulse Sequence

All experiments were performed on a General Electric EXCITE 3T (Waukesha, WI) clinical scanner equipped with 40 mT/m, 150 mT/m/ms gradients and a broadband radiofrequency amplifier. The radiofrequency coils used were custom-built, dual-tuned,  $^1\text{H}/^{13}\text{C}$  transmit/receive designs that were employed in previous studies (6,7,12,13,21,24). For all experiments,  $^{13}\text{C}$  spectra were overlaid on  $T_2$ -weighted proton images collected with a fast spin-echo sequence. Acquisition parameters for phantom axial proton images were a field of view (FOV) of 11 cm,  $256 \times 192$  matrix, 3mm slice thickness, and number of averages = 6. Mouse proton axial images were acquired with a FOV of 8 cm,  $192 \times 192$  matrix, 2mm slice thickness, and number of averages = 6. Coronal images for the mouse were the same, except FOV was 10 cm and slice thickness was 1.5mm. The  $^{13}\text{C}$  3D-MRSI spectra were acquired with the pulse sequence shown in Fig. 3a. The base sequence with adiabatic refocusing

FIG. 4. Results from phantom experiments. The upper left shows an image of a slice from a cylindrical phantom with spheres containing  $^{13}\text{C}$ -labeled alanine, pyruvate/pyruvate-hydrate, and lactate. The adjacent boxes show comparisons of spectral grids from 3D-MRSI acquisitions with no undersampling,  $\times 3.37$  undersampling, and  $\times 7.53$  undersampling. The  $16 \times 16$  voxels shown have  $3.75 \text{ mm} \times 3.75 \text{ mm}$  in-plane resolution. The  $6 \times 6$  grids to the right show spectra from the alanine sphere only (frequency axis zoomed in). The  $\ell_1$  reconstructions for the accelerated acquisitions matched the unaccelerated acquisition, showing high spectral quality and the preservation of small peaks. [Color figure can be viewed in the online issue, which is available at [www.interscience.wiley.com](http://www.interscience.wiley.com).]



pulses and fly-back readout has been described in detail previously (24). In short, this sequence selects a slab in  $z$ , phase-encode localizes in  $x$  and  $y$ , and uses a fly-back waveform to read out full echo data in  $z$  and frequency for each  $x/y$  phase encode. Specific sequence parameters for phantom and in vivo experiments are given below. As was done previously (7,12,21),  $k_x$ - $k_y$  data (in this case,  $k_x$ - $k_y$  blocks) were collected outward from the  $k$ -space origin in concentric order. In addition, a variable flip angle scheme (26), i.e., increasing flip angle over time to compensate for the loss in hyperpolarized signal and ending with a  $90^\circ$  pulse, was used in the in vivo experiments. The actual  $n^{\text{th}}$  flip angle  $\theta[n]$  precalculated by the source code for a given acquisition of  $N$  flips was as follows:

$$\theta[n] = \begin{cases} 90^\circ & \text{if } n = N \\ \arctan(\sin(\theta[n+1])) & \text{if } n < N \end{cases} \quad [4]$$

For example, in an acquisition with 64 readouts,  $\theta(64) = 90^\circ$ ,  $\theta(63) = \arctan(\sin(90^\circ)) = 45^\circ$ ,  $\theta(62) = \arctan(\sin(45^\circ)) = 35.3^\circ$ , ...  $\theta(1) = 7.2^\circ$ . Calibration for mouse scans was performed before each experiment using a small  $^{13}\text{C}$  external standard placed with the animal in the coil. The blips in Fig. 3a had a width of 0.8 ms (time between fly-back flat portions being 1.16 ms), and their placement and amplitudes were set to achieve the desired sampling patterns.

## Reconstruction

The steps to process undersampled  $^{13}\text{C}$  3D-MRSI data have been described previously (21). The major steps were as follows: (1) the readout data were reordered to pick out the data from flat portions of the fly-back readout and organize all the data into a 4D  $k_f$ - $k_x$ - $k_y$ - $k_z$  array, (2) the missing  $k$ -space data in each undersampled  $k_f$ - $k_x$ - $k_y$  set were filled in with the iterative nonlinear  $\ell_1$  algorithm described previously (20), and (3) standard proc-

essing was performed, including apodization, linear phase correction for the fly-back's tilted  $k$ -space trajectory (25), and a 4D Fourier transform. Step 2 was the additional component beyond conventional processing needed to account for the missing data from undersampling. For all phantom and mouse experiments, the  $\ell_1$  reconstruction parameters were the same as for the simulations, namely,  $\lambda = 0.0005$  (wavelet transform weight) and  $\alpha = 0.0001$  (total variation penalty weight).

## Phantom

Figure 4 shows a proton image of a slice from the cylindrical phantom used to experimentally validate our acceleration schemes. The phantom contained three spheres filled with different  $^{13}\text{C}$ -labeled compounds, pyruvate/pyruvate-hydrate in one, alanine in another, and lactate in the third. The validation consisted of comparing unaccelerated and accelerated 3D-MRSI acquisitions. For both, a flip angle of  $10^\circ$ , echo time = 140 ms, pulse repetition time = 2 sec, in-plane FOV =  $6 \text{ cm} \times 6 \text{ cm}$ ,  $16 \times 16$  phase encode matrix, 1-cm fly-back  $z$  resolution, 581-Hz spectral FOV, 9.8-Hz spectral resolution, concentric phase encode order, and number of averages = 16 were used with the sequence shown in Fig. 3a. The accelerated acquisitions used the  $\times 3.37$  and  $\times 7.53$  undersampling designs.

## Animals

All animal studies were carried out under a protocol approved by the UCSF Institutional Animal Care and Use Committee. For all in vivo experiments, a Hyper-sense<sup>TM</sup> dynamic nuclear polarization polarizer (Oxford Instruments, Abingdon, UK) was used. Twenty-four microliters (about 30 mg) of  $[1-^{13}\text{C}]$ pyruvic acid with 15 mM OX63 trityl radical, along with 0.5 mM (about  $0.47 \mu\text{L}$ ) of Prohance gadolinium for polarization enhancement (27), was polarized for 1 h in a field of 3.35 T at  $1.4^\circ\text{K}$ , with irradiation by 94.097-GHz (determined by

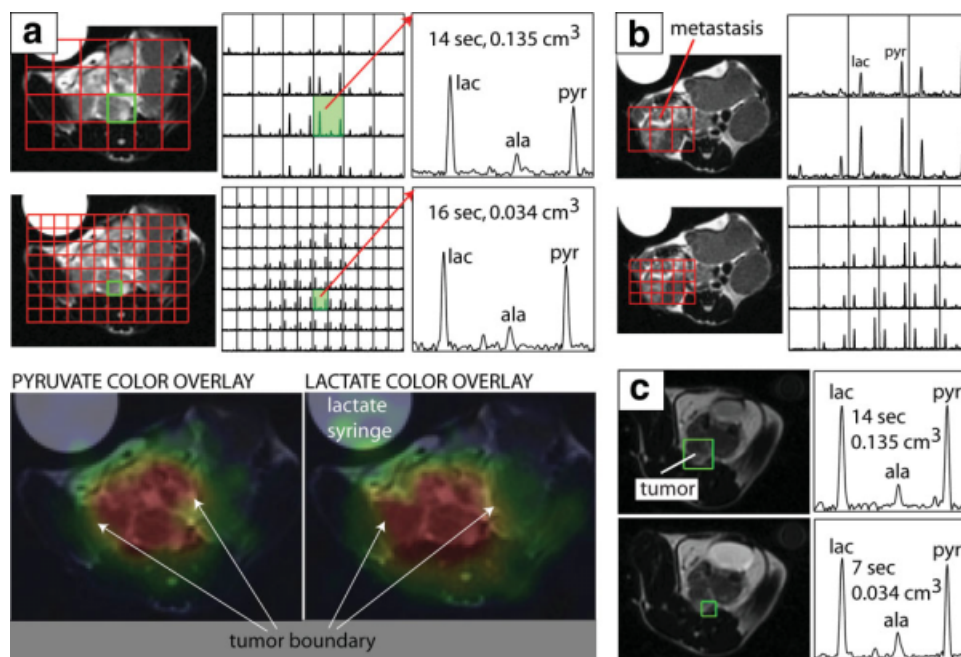


FIG. 5. **a:** In vivo validation in a transgenic mouse model of prostate cancer showing a comparison of spectra from an unaccelerated acquisition and an accelerated one with a quarter the voxel size and acquired in about the same time. The accelerated acquisition with higher resolution allowed for better delineation of the mouse body and better depiction of tumor heterogeneity. The spectra in the accelerated acquisition were of high quality, and small peaks were preserved. The color overlay maps generated from the accelerated spectra show high-intensity regions as brightly colored and highlight the spatial localization of metabolites according to tissue type. Tumor and nontumor regions showed clear differences in metabolic profile, and the boundaries were clearly delineated. **b:** A comparison of spectra from a different slice in the same mouse, with the higher-resolution spectra depicting heterogeneity and the boundaries of a metastasis better than the lower-resolution spectra. The full 3D acquisition allowed for imaging disease in multiple slices. **c:** High-quality spectra from a different prostate cancer mouse in which the  $\times 7.53$  accelerated sequence was used to quadruple resolution and nearly halve acquisition time. Once again, small peaks were preserved. [Color figure can be viewed in the online issue, which is available at [www.interscience.wiley.com](http://www.interscience.wiley.com).]

a frequency sweep) microwaves at 20-mW power. The dissolution medium consisted of an aqueous solution with 40 mM Tris, 80 mM NaOH, and 0.1 g/L Na<sub>2</sub>EDTA (ethylenediaminetetraacetic acid). The final dissolved material had a concentration of 80 mM, pH  $\sim 7.5$ , and a polarization  $\sim 25\%$  (measured by taking a small aliquot and injecting it into a custom-built polarimeter  $\sim 15$  sec after dissolution). Three hundred fifty microliters was injected into mice through either a jugular or tail vein catheter, followed by a 150- $\mu$ L saline flush. Detailed descriptions of our mouse-handling procedures, e.g., keeping animals warm and administering anesthesia, have been given previously (7,12). Two different animal models were used in our studies. The first was a transgenic adenocarcinoma of mouse prostate model (28,29) that we have used previously for hyperpolarized  $^{13}\text{C}$  spectroscopic imaging studies of cancer (7,12,21). The other model was a Tet-o-MYC/LAP-tTA double transgenic mouse model of liver cancer in which the human MYC proto-oncogene is overexpressed only in the liver (30,31). Liver cancer is a new preclinical application for hyperpolarized  $^{13}\text{C}$  studies and is potentially an attractive clinical target for rapid hyperpolarized spectroscopic imaging. The  $\times 3.37$  and  $\times 7.53$  accelerated patterns described above were used in the in vivo experiments both to increase spatial resolution and decrease scan time. The  $^{13}\text{C}$  3D-MRSI parameters were variable flip

angle, echo time = 140 ms, pulse repetition time = 215 ms, in-plane FOV = 4 cm  $\times$  4 cm, 16  $\times$  16 phase encode matrix, 5.4mm fly-back z resolution, 581-Hz spectral FOV, 9.8-Hz spectral resolution, and concentric phase-encode order. The lower-resolution unaccelerated acquisitions used an 8  $\times$  8 phase-encode matrix.

## RESULTS

### Phantom

Figure 4 shows a comparison of unaccelerated,  $\times 3.37$  accelerated, and  $\times 7.53$  accelerated acquisitions. The alanine sphere subset, with the frequency axis zoomed in, is also shown. The  $\ell_1$  reconstructed compressed sensing spectra were of high quality, matching up closely in spatial and spectral characteristics with the unaccelerated data. In addition, small peaks along the edges of the balls were accurately preserved. These peaks had SNRs on the order of 10 to 20 in the unaccelerated spectra.

### Animal

Figure 5 shows in vivo validation of the  $\times 3.37$  and  $\times 7.53$  accelerated sequences in prostate cancer mice. Figure 5a compares a slice from an unaccelerated acquisition with 0.135-cm<sup>3</sup> voxel size acquired in 14 sec with the same slice from a  $\times 3.37$  accelerated acquisition with a quarter



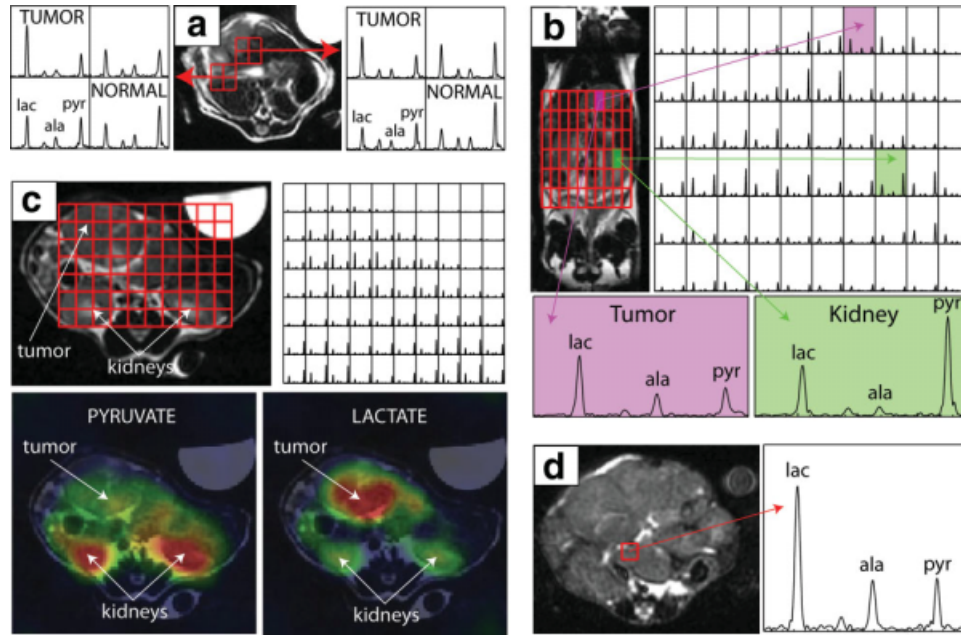


FIG. 6. **a**: Spectra from a transgenic liver cancer mouse with an early-stage tumor, as shown in the upper left of the anatomic image, in which acceleration was used to reduce voxel size by a factor of 4 ( $\times 3.37$  acceleration,  $0.034\text{-cm}^3$  voxel size, 16-sec acquisition). Tumor voxels exhibited dramatically elevated lactate/pyruvate ratios. The higher resolution reduced partial voluming such that distinct metabolic profiles were observed in tumor and adjacent tissue voxels. **b**: A separate data set in the same mouse with the same acquisition parameters in which the 3D-MRSI data are presented coronally to emphasize the distinct metabolic profiles in tumor and other tissues. **c**: A 3D-MRSI data set from a different mouse with a moderate-stage tumor at the level of the kidneys. Distinct differences between tumor and normal tissue are readily visualized in the color overlay maps. **d**: Data from a mouse with a large very late-stage tumor. Elevated alanine, as well as lactate, was detected in the tumor mass.

the voxel size acquired in 16 sec ( $\sim 1.5$  h between acquisitions). As shown in Fig. 5a, one benefit of the higher resolution afforded by the compressed sensing acquisition was better delineation of the outline of the mouse body. Even with the higher resolution, metabolic profiles were accurately preserved, as demonstrated by the highlighted voxels showing spectra from the same location for each acquisition. Small peaks such as alanine were reproduced and, interestingly, in this example, pyruvate hydrate (peak between lactate and alanine) was seen in the compressed sensing voxel. The bottom part of Fig. 5a shows pyruvate and lactate metabolite color maps generated from the accelerated spectra. Bright colors in the overlay map depict high-signal-intensity regions, allowing for easy visualization of the spatial localization of the metabolites. As demonstrated by these maps, pyruvate and lactate were localized to the tumor, and the tumor boundary was clearly delineated. Figure 5b shows a comparison of spectra from the kidney level in the same mouse where a metastasis was spotted, once again demonstrating better delineation of the mouse body due to higher resolution and also better depiction of the heterogeneity in tissue that was previously obscured by partial voluming. Figure 5a,b highlights an advantage of full volumetric spectroscopic imaging—gathering data from multiple planes and allowing for investigation of the relationship between organs, tumors, and metastases in those separate planes. Figure 5c shows *in vivo* data collected from a different prostate cancer mouse, providing another example of high-quality spectra obtained with the compressed sensing sequence. In the case of Fig. 5c, the

comparison was between a  $0.135\text{-cm}^3$  voxel from an unaccelerated acquisition of 14 sec and a voxel a quarter the size in the same anatomic location from a  $\times 7.53$  accelerated acquisition of 7 sec.

Figure 6 shows the first hyperpolarized spectroscopic images from a transgenic animal model of liver cancer (all examples with  $0.034\text{-cm}^3$  resolution,  $\times 3.37$  acceleration, and acquired in 16 sec). Figure 6a, depicting an early-stage liver tumor in the upper left quadrant of the anatomic image, once again highlights the benefits of the enhanced resolution from accelerated imaging, showing the reduction of partial voluming with smaller voxels. There was a clear difference between the tumor voxels (upper left in the spectral grids), which exhibited a high lactate/pyruvate ratio, and the normal tissue voxels (lower right in the spectral grids), which showed the opposite metabolic profile—a low lactate/pyruvate ratio. The other voxels showed an intermediate pattern, with lactate and pyruvate levels being comparable, presumably due to the tissue in those voxels containing a mixture of tumor and normal cells. Figure 6b, showing another 3D-MRSI data set from the same mouse but acquired on a different date, underscores the abnormal metabolic profile in tumor tissue. It presents a coronal overlay slice of the data to highlight the dramatically elevated lactate in the tumor, which was not found in other organs, such as the kidneys. Figure 6b highlights the fact that with 3D-MRSI, where data are acquired in three spatial dimensions, overlays in any of the anatomic planes—axial, coronal, and sagittal—are readily available. Figure 6c shows another data set acquired from a different mouse in which a moderate-stage liver tumor extended down to the



level of the kidneys, once again demonstrating differences in metabolic profiles, which are easily visualized in the color overlay maps. Figure 6d shows a representative voxel from a third transgenic liver mouse with a very large, late-stage tumor. As shown in Fig. 6d, both lactate/pyruvate and ala/pyruvate ratios were elevated in this mouse.

In summary, Figs. 5 and 6 show high-quality in vivo spectra from a total of five animals. Along with the phantom data, which matched simulations and showed high-quality comparisons between accelerated and unaccelerated acquisitions, these in vivo data provided further evidence of the feasibility and robustness of applying compressed sensing to hyperpolarized spectroscopic imaging.

## DISCUSSION

Hyperpolarized  $^{13}\text{C}$  spectroscopic imaging has several key properties that make it an ideal application for compressed sensing, namely, fundamental sparsity, high SNR, and a need for rapid imaging. Due to spin-lattice relaxation of hyperpolarized resonances to their thermal equilibrium levels,  $^{13}\text{C}$  hyperpolarized spectroscopy is more a time-limited modality than an SNR-limited one. In this work, we devised and implemented a pulse sequence methodology to achieve up to a factor of 7.53 in acceleration for 3D spectroscopic imaging. In addition, we performed simulation experiments to quantitatively assess the limits of acceleration and detectability. This simulation and pulse sequence framework enables the straightforward design and testing of compressed sensing acquisitions with higher accelerations as desired by the user and permitted by the application. We validated our designs with both phantom and in vivo experiments. The data from the MYC transgenic mouse model of liver cancer provided initial preclinical evidence of the feasibility of using hyperpolarized  $^{13}\text{C}$  technology for metabolic imaging of liver cancer. Hepatocellular carcinoma is estimated to cause a million deaths annually (32), and metastatic liver cancer is even more common. Novel targeted drug therapies are actively being developed (33), and metabolic imaging may play a significant role in assessing response to therapy. Hyperpolarized technology could become an important radiologic modality for the liver because of the ability to acquire metabolic images during a breath hold.

In the animal in vivo experiments presented in this work, compressed sensing acceleration was used to improve spatial resolution (to as fine as  $0.034\text{ cm}^3$ ) and decrease acquisition time. In eventual clinical applications, compressed sensing could instead be used to cover a larger FOV. For example, for human liver imaging, to cover FOVs from 32 cm up to 64 cm, with 1-cm resolution,  $32 \times 32$  to  $64 \times 64$  phase-encode matrices would be needed. The clinical scenario has several implications for compressed sensing pulse sequence design. First, there might be more sparsity to exploit with larger matrix sizes, and higher accelerations could result simply due to more room for undersampling. To achieve higher acceleration, blips would need to jump a greater number of phase-encode steps. Examining straightforward relations ( $\Delta k = (\gamma/2\pi) \cdot \text{blip area} = \frac{1}{\text{FOV}} \cdot \text{blip area} = \frac{1}{2} \cdot G \cdot 0.8\text{ms}$ ) and using the animal experiment parameters ( $\text{FOV} = 4\text{ cm}$ , blip width 0.8

ms, and carbon gyromagnetic ratio) indicates a gradient amplitude  $G = 0.58\text{ gauss/cm}$  to jump one phase-encode step  $\Delta k$  and  $1.75\text{ gauss/cm}$  to jump three phase-encode steps in the  $\times 7.53$  accelerated design. For the small FOVs in animal experiments, narrower blip widths could easily push the gradients close to the  $4\text{ gauss/cm}$  limit. Fortunately, FOVs in clinical applications would be about an order of magnitude larger, so gradient amplitude constraints would not pose major design limitations. In fact, in a clinical application, the blips could be made much narrower and be used with a symmetric instead of fly-back echo-planar readout. The symmetric readout would have an SNR efficiency advantage over the fly-back, especially given the low gyromagnetic ratio for carbon, though the fly-back readout is inherently less sensitive to many hardware imperfections (25). The minimum spatial resolution achievable in the fly-back dimension with our fly-back readout was  $5.4\text{mm}$ . Higher resolution would be possible with a symmetric readout, but it would probably not be needed in a clinical setting, where  $1\text{-cm}^3$  voxel sizes would likely be appropriate. Ultimately, a practical limitation on the resolution in a clinical setting might be set by another consideration, voxel SNR, which depends on the concentration of the substrate that can be safely administered.

To achieve even faster scans with our echo-planar readout, other options exist, e.g., removing the double spin-echo and coping with field inhomogeneity effects. Another avenue actively being investigated for accelerated imaging is the combination of compressed sensing with parallel imaging. Although our work focused on an echo-planar compressed sensing scheme, other detection approaches exist that may ultimately prove clinically valuable, e.g., spiral readouts (34,35). One proposed approach that would allow for very rapid acquisitions relies on a multiecho acquisition and matrix inversion reconstruction for parametric estimation of a known set of chemical species instead of using a full spectroscopic readout (36). Radial sampling incorporating a back-projection reconstruction (HighY constrained back PROjection) (37) represents yet another possibility, though it may be most applicable to dynamic MRSI where a composite image exists.

Hyperpolarized technology for the measurement of  $^{13}\text{C}$  metabolic flux has great potential as a clinically relevant imaging tool and has several advantages, including high SNR and no background signal. Significant preclinical evidence for the usefulness of the substrate [ $1\text{-}^{13}\text{C}$ ]pyruvate has already been shown (5,7,8,12). These results are not surprising, given the Warburg hypothesis and the central role of lactate in the anaerobic metabolism characteristic of many cancers (38). Hyperpolarized technology also has flexibility in terms of the pathways that can be probed, as demonstrated by ongoing efforts to polarize new compounds (13–15). The sequence development in this project applying compressed sensing should be generally applicable for other hyperpolarized agent imaging studies as well.

## CONCLUSIONS

In this work, a method for applying compressed sensing to hyperpolarized  $^{13}\text{C}$  3D spectroscopic imaging was

presented and validated in simulations, phantom experiments, and in vivo studies, with up to a factor of 7.53 in acceleration demonstrated. In addition,  $^{13}\text{C}$  hyperpolarized data from a transgenic model of liver cancer were collected throughout the animal at higher spatial resolution ( $0.034\text{ cm}^3$ ) than previous 3D-MRSI acquisitions.

## ACKNOWLEDGMENTS

We thank Dr. James Tropp for designing and building the coils used in this study and Kristen Scott for her assistance during the in vivo experiments. This study was supported by the UCSF Program for Breakthrough Biomedical Research.

## REFERENCES

- Ardenkjaer-Larsen JH, Fridlund B, Gram A, Hansson G, Hansson L, Lerche MH, Servin R, Thaning M, Golman K. Increase in signal-to-noise ratio of  $>10,000$  times in liquid-state NMR. *Proc Natl Acad Sci USA* 2003;100:10158–10163.
- Wolber J, Ellner F, Fridlund B, Gram A, Johannesson H, Hansson G, Hansson LH, Lerche MH, Mansson S, Servin R, Thaning M, Golman K, Ardenkjaer-Larsen JH. Generating highly polarized nuclear spins in solution using dynamic nuclear polarization. *Nucl Instrum Methods Phys Res A* 2004;526:173–181.
- Golman K, Zandt R, Thaning M. Real-time metabolic imaging. *Proc Natl Acad Sci USA* 2006;103:11270–11275.
- Golman K, Peterson JS. Metabolic imaging and other applications of hyperpolarized  $^{13}\text{C}$ . *Acad Radiol* 2006;13:932–942.
- Golman K, Zandt R, Lerche M, Pehrson R, Ardenkjaer-Larsen JH. Metabolic imaging by hyperpolarized  $^{13}\text{C}$  magnetic resonance imaging for in vivo tumor diagnosis. *Cancer Res* 2006;66:10855–10860.
- Kohler SJ, Yen Y, Wolber J, Chen AP, Albers MJ, Bok R, Zhang V, Tropp J, Nelson SJ, Vigneron DB, Kurhanewicz J, Hurd RE. In vivo  $^{13}\text{C}$  carbon metabolic imaging at 3T with hyperpolarized  $^{13}\text{C}$ -1-pyruvate. *Magn Reson Med* 2007;58:65–69.
- Chen AP, Albers MJ, Cunningham CH, Kohler SJ, Yen Y, Hurd RE, Tropp J, Bok R, Pauly JM, Nelson SJ, Kurhanewicz J, Vigneron DB. Hyperpolarized C-13 spectroscopic imaging of the TRAMP mouse at 3T: initial experience. *Magn Reson Med* 2007;58:1099–1106.
- Day SE, Kettunen MI, Gallagher FA, Hu DE, Lerche M, Wolber J, Golman K, Ardenkjaer-Larsen JH, Brindle KM. Detecting tumor response to treatment using hyperpolarized  $^{13}\text{C}$  magnetic resonance imaging and spectroscopy. *Nat Med* 2007;13:1382–1387.
- Merritt ME, Harrison C, Storey C, Jeffrey FM, Sherry AD, Malloy CR. Hyperpolarized  $^{13}\text{C}$  allows a direct measure of flux through a single enzyme-catalyzed step by NMR. *Proc Natl Acad Sci USA* 2007;104:19773–19777.
- Schroeder MA, Cochlin LE, Heather LC, Clarke K, Radda GK, Tyler DJ. In vivo assessment of pyruvate dehydrogenase flux in the heart using hyperpolarized carbon-13 magnetic resonance. *Proc Natl Acad Sci USA* 2008;105:12051–12056.
- Merritt ME, Harrison C, Storey C, Sherry AD, Malloy CR. Inhibition of carbohydrate oxidation during the first minute of reperfusion after brief ischemia: NMR detection of hyperpolarized  $^{13}\text{CO}_2$  and  $\text{H}^{13}\text{CO}_3^-$ . *Magn Reson Med* 2008;60:1029–1036.
- Albers MJ, Bok R, Chen AP, Cunningham CH, Zierhut ML, Zhang V, Kohler SJ, Tropp J, Hurd RE, Yen Y, Nelson SJ, Vigneron DB, Kurhanewicz J. Hyperpolarized  $^{13}\text{C}$  lactate, pyruvate, and alanine: noninvasive biomarkers for prostate cancer detection and grading. *Cancer Res* 2008;68:8607–8615.
- Chen AP, Kurhanewicz J, Bok R, Xu D, Joun D, Zhang V, Nelson SJ, Hurd RE, Vigneron DB. Feasibility of using hyperpolarized  $[\text{l-}^{13}\text{C}]\text{lactate}$  as a substrate for in vivo metabolic  $^{13}\text{C}$  MRSI studies. *Magn Reson Imaging* 2008;26:721–726.
- Gallagher FA, Kettunen MI, Day SE, Lerche M, Brindle KM.  $^{13}\text{C}$  MR spectroscopy measurements of glutaminase activity in human hepatocellular carcinoma cells using hyperpolarized  $^{13}\text{C}$ -labeled glutamine. *Magn Reson Med* 2008;60:253–257.
- Gallagher FA, Kettunen MI, Day SE, Hu DE, Ardenkjaer-Larsen JH, Zandt R, Jensen PR, Karlsson M, Golman K, Lerche MH, Brindle KM. Magnetic resonance imaging of pH in vivo using hyperpolarized  $^{13}\text{C}$ -labelled bicarbonate. *Nature* 2008;453:940–944.
- Candes E, Romberg J, Tao T. Robust uncertainty principles: exact reconstruction from highly incomplete information. *IEEE Trans Inform Theory* 2006;52:489–509.
- Donoho DL. Compressed sensing. *IEEE Trans Inform Theory* 2006;52:1289–1306.
- Candes E, Romberg J. Signal recovery from random projections. *Proc SPIE-IS&T* 2005;5674:76–86.
- Tsaig Y, Donoho DL. Extensions of compressed sensing. *Signal Processing* 2006;86:549–571.
- Lustig M, Donoho DL, Pauly JM. Sparse MRI: the application of compressed sensing for rapid MR imaging. *Magn Reson Med* 2007;58:1182–1195.
- Hu S, Lustig M, Chen AP, Crane J, Kerr A, Kelley DAC, Hurd R, Kurhanewicz J, Nelson SJ, Pauly JM, Vigneron DB. Compressed sensing for resolution enhancement of hyperpolarized  $^{13}\text{C}$  flyback 3D-MRSI. *J Magn Reson* 2008;192:258–264.
- Stern AS, Donoho DL, Hoch JC. NMR data processing using iterative thresholding and minimum l1-norm reconstruction. *J Magn Reson* 2007;188:295–300.
- Candes EJ, Wakin MB, Boyd SP. Enhancing sparsity by reweighted l1 minimization. *J Fourier Anal Appl* 2008;14:877–905.
- Cunningham CH, Chen AP, Albers MJ, Kurhanewicz J, Hurd RE, Yen Y, Pauly JM, Nelson SJ, Vigneron DB. Double spin-echo sequence for rapid spectroscopic imaging of hyperpolarized  $^{13}\text{C}$ . *J Magn Reson* 2007;187:357–362.
- Cunningham CH, Vigneron DB, Chen AP, Xu D, Nelson SJ, Hurd RE, Kelley DA, Pauly JM. Design of flyback echo-planar readout gradients for magnetic resonance spectroscopic imaging. *Magn Reson Med* 2005;54:1286–1289.
- Zhao L, Mulkern R, Tseng C, Williamson D, Patz S, Kraft R, Walsworth RL, Jolesz FA, Albert MS. Gradient-echo imaging considerations for hyperpolarized  $^{129}\text{Xe}$  MR. *J Magn Reson B* 1996;113:179–183.
- Ardenkjaer-Larsen JH, Macholl S, Johannesson H. Dynamic nuclear polarization with trityls at 1.2 K. *Appl Magn Reson* 2008;34:509–522.
- Greenberg NM, DeMayo F, Finegold MJ, Medina D, Tilley WD, Aspinall JO, Cunha GR, Donjacour AA, Matusik RJ, Rosen JM. Prostate cancer in a transgenic mouse. *Proc Natl Acad Sci USA* 1995;92:3439–3443.
- Kaplan-Lefko PJ, Chen TM, Ittmann MM, Barrios RJ, Ayala GE, Huss WJ, Maddison LA, Foster BA, Greenberg NM. Pathobiology of autochthonous prostate cancer in a pre-clinical transgenic mouse model. *Prostate* 1993;55:219–237.
- Shachaf CM, Kopelman AM, Arvanitis C, Karlsson A, Beer S, Mandl S, Bachmann MH, Borowsky AD, Ruebner B, Cardiff RD, Yang Q, Bishop JM, Contag CH, Felsher DW. MYC inactivation uncovers pluripotent differentiation and tumour dormancy in hepatocellular cancer. *Nature* 2004;431:1112–1117.
- Goga A, Yang D, Tward AD, Morgan DO, Bishop JM. Inhibition of CDK1 as a potential therapy for tumors over-expressing MYC. *Nat Med* 2007;13:820–827.
- Carr BI. Hepatocellular cancer. Totowa, NJ: Humana Press; 2005. 312 p.
- Tommasi S, Pinto R, Pilato B, Paradiso A. Molecular pathways and related target therapies in liver carcinoma. *Curr Pharm Des* 2007;13:3279–3287.
- Mayer D, Levin YS, Hurd RE, Glover GH, Spielman DM. Fast metabolic imaging of systems with sparse spectra: application for hyperpolarized  $^{13}\text{C}$  imaging. *Magn Reson Med* 2006;56:932–937.
- Levin YS, Mayer D, Hurd RE, Spielman DM. Optimization of fast spiral chemical shift imaging using least squares reconstruction: application for hyperpolarized  $^{13}\text{C}$  metabolic imaging. *Magn Reson Med* 2007;58:245–252.
- Leupold J, Mansson S, Petersson JS, Hennig J, Wieben O. Fast multi-echo balanced SSFP metabolite mapping of  $^1\text{H}$  and hyperpolarized  $^{13}\text{C}$  compounds. *MAGMA* 2009;22:251–256.
- Mistretta CA, Wieben O, Velikina J, Block W, Perry J, Wu Y, Johnson K, Wu Y. Highly constrained backprojection for time-resolved MRI. *Magn Reson Med* 2006;55:30–40.
- DeBerardinis RJ, Lum JJ, Hatzivassiliou G, Thompson CB. The biology of cancer: metabolic reprogramming fuels cell growth and proliferation. *Cell Metab* 2008;7:11–20.